J Eng Math (2013) 80:1–20
DOI 10.1007/s10665-013-9623-z

Asymptotic solutions of glass temperature profiles during steady optical fibre drawing

M. Taroni · C. J. W. Breward · L. J. Cummings · I. M. Griffiths

Received: 28 September 2012 / Accepted: 11 January 2013 / Published online: 12 March 2013

Abstract In this paper we derive realistic simplified models for the high-speed drawing of glass optical fibres via the downdraw method that capture the fluid dynamics and heat transport in the fibre via conduction, convection and radiative heating. We exploit the small aspect ratio of the fibre and the relative orders of magnitude of the dimensionless parameters that characterize the heat transfer to reduce the problem to one- or two-dimensional systems via asymptotic analysis. The resulting equations may be readily solved numerically and in many cases admit exact analytic solutions. The systematic asymptotic breakdown presented is used to elucidate the relative importance of furnace temperature profile, convection, surface radiation and conduction in each portion of the furnace and the role of each in controlling the glass temperature. The models derived predict many of the qualitative features observed in real industrial processes, such as the glass temperature profile within the furnace and the sharp transition in fibre thickness. The models thus offer a desirable route to quick scenario testing, providing valuable practical information about the dependencies of the solution on the parameters and the dominant heat-transport mechanism.

Keywords Asymptotic analysis · Extensional flow · Heat transfer · Optical fibre drawing · Slow viscous flow

1 Introduction

Fibre drawing is an important industrial process used to manufacture fibre-optic cables for telecommunications applications. A cylindrical glass preform, of diameter around 5 cm, is lowered into a furnace. Here the preform

M. Taroni · C. J. W. Breward · I. M. Griffiths (✉)
Oxford Centre for Collaborative Applied Mathematics, Mathematical Institute, University of Oxford, 24-29 St Giles', Oxford OX1 3LB, UK
e-mail: griffit4@maths.ox.ac.uk

M. Taroni
e-mail: taroni@maths.ox.ac.uk

C. J. W. Breward
e-mail: breward@maths.ox.ac.uk

L. J. Cummings
Department of Mathematical Sciences, New Jersey Institute of Technology, Newark, NJ 07102, USA
e-mail: linda.cummings@njit.edu

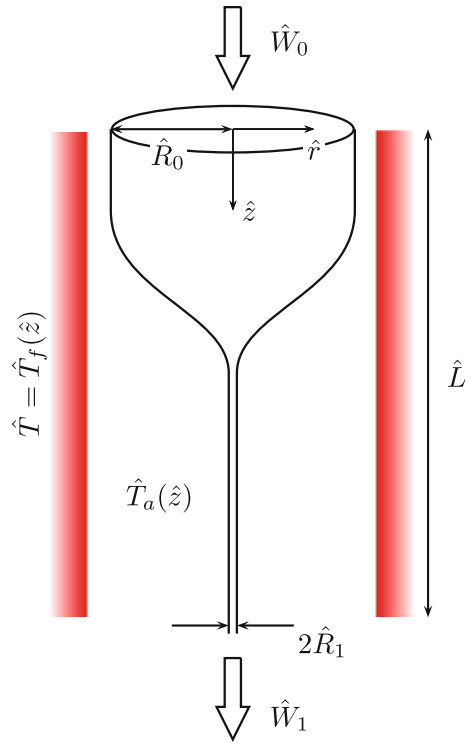

Fig. 1 Schematic diagram for drawing of optical glass fibres. The (dimensional) furnace temperature is given by $\hat{T}_f(\hat{z})$, whereas the ambient air temperature in the furnace is denoted by $\hat{T}_a(\hat{z})$

melts, the glass viscosity decreases, and a fibre of thickness around 100 μm may be drawn by applying a tension at the end. As it exits the furnace, the glass is cooled by the air and solidifies into the desired solid fibre. A schematic of the process is shown in Fig. 1.

One of the most interesting aspects of the process is that it is not isothermal, and many of the material properties, most notably the glass viscosity, are found to depend on the temperature. In general, the glass temperature is governed by a balance between thermal convection, radiation and conduction, although the relative importance of these effects changes with distance down the fibre. In particular, there is typically a sharp transition in the glass thickness, with the glass behaving differently on either side of the transition point.

There have been many theoretical studies of the drawing process in the literature stretching back over 40 years. Early work considered the one-dimensional problem, in which quantities of interest vary only in the axial direction and not radially [8,14]. Later studies concentrated on improving the modelling of the radiative heat transfer [13], with Jaluria and co-workers gradually developing methods to solve the full three-dimensional conjugate heat transfer between the glass, surrounding gas and furnace [11,18]. However, these solutions are computationally very demanding, and so simpler models remain desirable for quick scenario testing and to give clearer insight into the dependencies of the solution on the parameters. To that end, Huang and co-workers extended earlier one-dimensional models to investigate the effects of, for example, viscous dissipation [22] and dopant diffusion [9], but often at the expense of realistic radiative modelling, which is an inherent part of the industrial process. Other studies ignored radiative heating altogether and considered only the cooling stage of the process [15]. Further, the majority of work in this area considers fibre drawing with a draw speed of comparable magnitude with the input speed, whereas fabrication of thin optical fibres necessitates much higher draw speeds that have become possible more recently [25].

In this paper we derive simplified but realistic models for high-speed fibre drawing for the fabrication of optical fibres, including both radiative and convective heat transfer throughout the process, and determine where each mechanism dominates. We exploit both the small aspect ratio of the fibre and the relative orders of magnitude of the dimensionless parameters to reduce the problem to a one- or two-dimensional system of equations that may be

readily solved numerically and for which some approximate analytical solutions exist. In particular, we aim to give a systematic asymptotic breakdown of the dependencies of convection, surface radiation and conduction and how their relative importance changes with axial distance down the furnace. We investigate different possible functional forms for the radius-dependent radiative and convective heat transfer coefficients and in addition consider the effect of non-uniform furnace temperatures.

The paper is laid out as follows. In § 2, we formulate our theoretical description of the problem, coupling together the axisymmetric slow-flow equations with an energy equation governing the temperature of the glass. In § 3, we exploit the small aspect ratio of the fibre to derive one-dimensional equations for the fluid flow. We then consider the temperature profiles of the glass in § 4, considering a number of different asymptotic limits that may be relevant to the industrial process. Finally, in § 5, we discuss our results and consider possible avenues for future research.

2 Problem description

2.1 Governing equations

2.1.1 Fluid flow

We consider the steady-state configuration where the input radius of the fibre preform is $\hat{R}_0$ and the length of the furnace is $\hat{L}$, as depicted in Fig. 1, and we note that for clarity all dimensional quantities are denoted with hats. Based on typical parameter values for the process (Table 1), we find that the Reynolds number for the flow, based on the fibre radius, is very small and, assuming axisymmetry, the fluid flow is governed by the slow-flow equations [5]:

$$\frac{1}{\hat{r}}\frac{\partial}{\partial \hat{r}}\left(\hat{r}\hat{u}\right)+\frac{\partial \hat{w}}{\partial \hat{z}}=0, \tag{1a}$$

$$-\frac{\partial \hat{p}}{\partial \hat{r}}+\frac{\partial}{\partial \hat{z}}\left(\hat{\mu}\frac{\partial \hat{u}}{\partial \hat{z}}\right)+\hat{\mu}\frac{\partial}{\partial \hat{r}}\left(\frac{1}{\hat{r}}\frac{\partial}{\partial \hat{r}}\left(\hat{r}\frac{\partial \hat{u}}{\partial \hat{r}}\right)\right)+\frac{\partial \hat{\mu}}{\partial \hat{z}}\frac{\partial \hat{w}}{\partial \hat{r}}+2\frac{\partial \hat{\mu}}{\partial \hat{r}}\frac{\partial \hat{u}}{\partial \hat{r}}=0, \tag{1b}$$

$$-\frac{\partial \hat{p}}{\partial \hat{z}}+\frac{\partial}{\partial \hat{z}}\left(2\hat{\mu}\frac{\partial \hat{w}}{\partial \hat{z}}\right)+\frac{1}{\hat{r}}\frac{\partial}{\partial \hat{r}}\left(\hat{\mu}\hat{r}\frac{\partial \hat{w}}{\partial \hat{r}}\right)+\frac{1}{\hat{r}}\frac{\partial}{\partial \hat{r}}\left(\hat{\mu}\hat{r}\frac{\partial \hat{u}}{\partial \hat{z}}\right)=0, \tag{1c}$$

where $\hat{r}$ and $\hat{z}$ denote the radial and axial coordinates, $\hat{p}$ is the pressure within the molten glass, and $\hat{u}$ and $\hat{w}$ are the radial and axial velocities of the glass. The glass viscosity, denoted $\hat{\mu}$, is a function of its temperature $\hat{T}$ only, which may in general vary both along and across the fibre. At the centre of the fibre, symmetry provides the conditions

$$\hat{u}=\frac{\partial \hat{w}}{\partial \hat{r}}=0 \tag{2a}$$

on $\hat{r}=0$, while the kinematic and dynamic boundary conditions are

$$\hat{u}=\hat{w}\frac{\mathrm{d}\hat{R}}{\mathrm{d}\hat{z}}, \tag{2b}$$

$$\left(-\hat{p}+2\hat{\mu}\frac{\partial \hat{u}}{\partial \hat{r}}\right)=\hat{\mu}\frac{\mathrm{d}\hat{R}}{\mathrm{d}\hat{z}}\left(\frac{\partial \hat{u}}{\partial \hat{z}}+\frac{\partial \hat{w}}{\partial \hat{r}}\right), \tag{2c}$$

$$\hat{\mu}\left(\frac{\partial \hat{u}}{\partial \hat{z}}+\frac{\partial \hat{w}}{\partial \hat{r}}\right)=\frac{\mathrm{d}\hat{R}}{\mathrm{d}\hat{z}}\left(-\hat{p}+2\hat{\mu}\frac{\partial \hat{w}}{\partial \hat{z}}\right) \tag{2d}$$

on the glass–air interface $\hat{r}=\hat{R}(\hat{z})$, where we neglect any effects due to surface tension since these are typically small [9]. The fluid problem is closed by specifying the velocity at the two ends of the tubing,

$$\hat{w}(\hat{r},\hat{z}=0)=\hat{W}_0,\quad \hat{w}(\hat{r},\hat{z}=\hat{L})=\hat{W}_1. \tag{2e}$$

Table 1 Typical parameter values for high-speed drawing of glass fibres

Parameter	Symbol	Approximate value	Units
Tubing length[a,b]	$\hat{L}$	0.5	m
Initial radius[a]	$\hat{R}_0$	0.05	m
Input speed[a]	$\hat{W}_0$	10^{-3}	$\mathrm{m\,s^{-1}}$
Draw speed[a]	$\hat{W}_1$	30	$\mathrm{m\,s^{-1}}$
Density[b,c]	$\hat{\rho}$	2200	$\mathrm{kg\,m^{-3}}$
Furnace temperature[d,e]	$\hat{T}_\mathrm{f}$	3000	K
Ambient air temperature[d,e]	$\hat{T}_\mathrm{a}$	2250	K
Glass softening temperature[d,e]	$\hat{T}_s$	1900	K
Softening viscosity[e]	$\hat{\mu}_s$	4500	$\mathrm{N\,s\,m^{-2}}$
Specific heat[b,c,e]	$\hat{c}_p$	1000	$\mathrm{J\,kg^{-1}\,K^{-1}}$
Heat transfer coefficient[b,c,e]	$\hat{k}_h$	100	$\mathrm{W\,m^{-2}}$
Thermal conductivity[b,e]	$\hat{k}_c$	1.1	$\mathrm{W\,m^{-1}\,K^{-1}}$
Stefan–Boltzmann constant[e]	$\hat{\sigma}$	5.67×10^{-8}	$\mathrm{W\,m^{-2}\,K^{-4}}$
Specific emissivity[d]	ε_r	0.9	–
Refractive index[e]	n_0	1.5	–
Absorption coefficient[c,d]	$\hat{\chi}$	200	$\mathrm{m^{-1}}$

[a] Yin and Jaluria [25]
[b] Huang et al. [9]
[c] Paek and Runk [14]
[d] Myers [13]
[e] Lee and Jaluria [11]

2.1.2 Glass viscosity

The viscosity of glass varies significantly with temperature, with a number of expressions for $\hat{\mu}(\hat{T})$ having been reported in the literature depending on the type of glass [8]. We choose

$$\hat{\mu} = \hat{\mu}_s \exp\left(a\left(\frac{1}{\hat{T}} - \frac{1}{\hat{T}_s}\right)\right), \tag{3}$$

which is suitable for fused silica, where $\hat{T}_s$ is the softening temperature for glass, $\hat{\mu}_s$ the softening viscosity, and a an empirically determined constant [13].

2.1.3 Temperature equation

The equation governing the distribution of temperature is

$$\hat{\rho}\hat{c}_p\left(\hat{u}\frac{\partial\hat{T}}{\partial\hat{r}} + \hat{w}\frac{\partial\hat{T}}{\partial\hat{z}}\right) = \frac{1}{\hat{r}}\frac{\partial}{\partial\hat{r}}\left(\hat{k}(\hat{T})\hat{r}\frac{\partial\hat{T}}{\partial\hat{r}}\right) + \frac{\partial}{\partial\hat{z}}\left(\hat{k}(\hat{T})\frac{\partial\hat{T}}{\partial\hat{z}}\right), \tag{4}$$

where the left-hand side represents thermal convection and the right-hand side thermal conduction, with $\hat{k}(\hat{T})$ denoting the conductivity of glass. For transparent materials, radiative transfer within the material is of significance, especially at high temperatures. A full description of this effect is a formidable challenge; however, provided the fibre is *optically thick*, that is, $\hat{R}$ is much greater than the absorption length scale, $1/\hat{\chi}$, where $\hat{\chi}$ is the glass absorption coefficient (with typical values given in Table 1), one may use the Rosseland approximation to include a radiative contribution to the thermal conductivity, $\hat{k}_c$, so that the apparent conductivity $\hat{k}(\hat{T}) = \hat{k}_c + \hat{k}_r(\hat{T})$, where [14]

$$\hat{k}_r(\hat{T}) = \frac{16n_0^2\hat{\sigma}\hat{T}^3}{3\hat{\chi}}. \tag{5}$$

Here $\hat{\sigma}$ is the Stefan–Boltzmann constant and n_0 denotes the refractive index for the glass (with typical values given in Table 1). We may therefore separate the respective conductive components in (4) to give

$$\hat{\rho}\hat{c}_p\left(\hat{u}\frac{\partial\hat{T}}{\partial\hat{r}} + \hat{w}\frac{\partial\hat{T}}{\partial\hat{z}}\right) = \frac{1}{\hat{r}}\frac{\partial}{\partial\hat{r}}\left(\hat{k}_c\hat{r}\frac{\partial\hat{T}}{\partial\hat{r}}\right) + \frac{\partial}{\partial\hat{z}}\left(\hat{k}_c\frac{\partial\hat{T}}{\partial\hat{z}}\right) + \frac{1}{\hat{r}}\frac{\partial}{\partial\hat{r}}\left(\hat{\kappa}_r(\hat{T})\hat{r}\frac{\partial\hat{T}^4}{\partial\hat{r}}\right) + \frac{\partial}{\partial\hat{z}}\left(\hat{\kappa}_r(\hat{T})\frac{\partial\hat{T}^4}{\partial\hat{z}}\right), \tag{6}$$

where $\hat{\kappa}_r(\hat{T}) = \hat{k}_r/4\hat{T}^3$. The assumption may break down once the fibre is drawn down to a thickness of $O(100\,\mu\text{m})$, at which point one might expect the glass to absorb the radiation directly from the surrounding furnace and re-radiate heat back to the furnace.[1] Nevertheless, given that the absorption length scale is highly dependent on the glass properties and radiation wavelength, in the interest of simplicity we limit ourselves to considering only the optically thick limit. Furthermore, we note that the validity of the Rosseland approximation for the fibre-drawing process has been confirmed by numerical tests using more realistic models for bulk radiation [24].

The boundary condition at the glass–air interface $\hat{r} = \hat{R}(\hat{z})$ is

$$-\hat{k}\frac{\partial \hat{T}}{\partial \hat{r}} = \hat{\sigma}\varepsilon_r\left(\hat{T}^4 - \hat{T}_\text{f}^4\right) + \hat{k}_h\left(\hat{T} - \hat{T}_\text{a}\right), \tag{7}$$

where $\hat{T}_\text{f} = \hat{T}_\text{f}(\hat{z})$ and $\hat{T}_\text{a} = \hat{T}_\text{a}(\hat{z})$ are, respectively, the temperatures of the furnace and ambient air in the furnace, both of which are assumed to be known functions of the distance along the furnace, as discussed in § 2.1.4. The terms on the right-hand side represent respectively radiative transfer and convective heating to the surroundings via Newton cooling [1]. Here ε_r is the specific emissivity and $\hat{k}_h$ the heat transfer coefficient, which may depend on the radius of the fibre; appropriate functional forms are discussed in § 2.1.5.

Finally, the system is closed by specifying the input temperature $\hat{T} = \hat{T}_0$ at $\hat{z} = 0$. For simplicity, we assume that $\hat{T}_0$ is a constant so that the heat flux through the outer radius is zero. Then (7) implies that $\hat{T}_0$ is given by the solution to the quartic equation

$$\hat{\sigma}\varepsilon_r\left(\hat{T}_0^4 - \hat{T}_\text{f}(0)^4\right) + \hat{k}_h\left(\hat{T}_0 - \hat{T}_\text{a}(0)\right) = 0. \tag{8}$$

However, in reality, the temperature of the glass entering the furnace is unlikely to satisfy (8); rather, the fibre will enter at the far lower ambient temperature outside the furnace, say around 300 K. In this case we expect there to be a small transient near the inlet over which the system quickly adjusts to the solution of (8). We investigate this thermal boundary layer in § 4.1.1.

2.1.4 The form of $\hat{T}_\text{f}$ and $\hat{T}_\text{a}$

The furnace temperature $\hat{T}_\text{f}$ is not very well characterized, but it is known that the furnace is generally hottest in the central portion and coolest at the ends [11] and has been typically modelled as having either a Gaussian or parabolic profile [17]. To evaluate the effect of the furnace temperature, we consider both an isothermal and varying temperature profile, with the latter taken to be of the functional form [4]

$$\hat{T}_\text{f}(\hat{z}) = \hat{T}_\text{m}\left(\tfrac{1}{5} + \tfrac{4}{5}\text{e}^{-0.5(\hat{z}/\hat{L}-0.35)^2}\right), \tag{9}$$

with the maximum temperature $\hat{T}_\text{m} \approx 3000\,\text{K}$.

For a given furnace profile, the ambient air temperature should be determined as part of the solution to the full heat transfer problem [18]. However, for simplicity we assume the ambient temperature to be known. Several authors take this to be constant, with $\hat{T}_\text{a} \approx \hat{T}_\text{m}/2$ [11,14], or equal to room temperature [9]. However, full numerical simulations suggest that $\hat{T}_\text{a}(\hat{z})$ follows the same profile as $\hat{T}_\text{f}(\hat{z})$, so we follow Filippov [4] and set $\hat{T}_\text{a}(\hat{z}) = 3\hat{T}_\text{f}(\hat{z})/4$ throughout.

2.1.5 The form of ε_r and $\hat{k}_\text{h}$

Although typical values for the specific emissivity ε_r and heat transfer coefficient $\hat{k}_\text{h}$ given in Table 1 are often treated as constant, they are in fact both dependent on the material properties, temperature and radius of the fibre. The emissivity is particularly tricky to measure at typical furnace temperatures and is usually assumed to behave as

[1] One can tackle this *optically thin* limit in an ad hoc manner by including an additional radiative term in the temperature Eq. (4), as was done by Fitt et al. [5].

if at room temperature, where it is experimentally found to decrease with decreasing fibre radius. While [14] posed an ad hoc smoothly varying $\varepsilon_r(\hat{R}) \in [0.1, 0.6]$, [13] derived a more accurate model with $\varepsilon_r(\hat{R}) \in (0, 0.9]$, reaching the higher value for $\hat{R} \gtrsim 1/\hat{\chi} \approx 10^{-2}$ m.

To maintain generality, we consider separately the cases of an emissivity that is constant and one that is of the functional form $\varepsilon_r \sim 1 - e^{-\phi\hat{R}}$, with $\phi \approx 2.5\hat{\chi}$ chosen so as to give qualitative agreement with Myers's model [13].

The heat transfer coefficient $\hat{k}_h$ is generally thought to vary only weakly throughout the process, although values between 10 and 300 Wm^{-2} have been reported in the literature. While it is generally taken to be constant, [6] and [8] have assumed the functional form $\hat{R}\hat{k}_h \sim (\hat{w}\hat{R})^{1/3}$, derived by considering flow past a cylinder. In this paper, we therefore investigate the effect of a $\hat{k}_h$ that is both constant and of the form posed by Geyling and Homsy [8].

2.2 Non-dimensionalization

We exploit the slenderness of the geometry, that is, we introduce the inverse aspect ratio $\epsilon = \hat{R}_0/\hat{L} \approx 0.1 \ll 1$ and scale using

$$\hat{r} = \epsilon\hat{L}r, \quad \hat{z} = \hat{L}z, \quad \hat{u} = \epsilon\hat{W}_0 u, \quad \hat{w} = \hat{W}_0 w,$$
$$\hat{R} = \epsilon\hat{L}R, \quad \hat{T} = \hat{T}_s T, \quad \hat{p} = \frac{\hat{\mu}_s\hat{W}_0}{\epsilon^2\hat{L}}p, \quad \hat{\mu} = \hat{\mu}_s\mu. \tag{10}$$

Substituting into (1) and (4) provides the dimensionless system

$$\frac{1}{r}\frac{\partial}{\partial r}(ru) + \frac{\partial w}{\partial z} = 0, \tag{11a}$$
$$-\frac{\partial p}{\partial r} + \epsilon^4\frac{\partial}{\partial z}\left(\mu\frac{\partial u}{\partial z}\right) + \epsilon^2\mu\frac{\partial}{\partial r}\left(\frac{1}{r}\frac{\partial}{\partial r}(ru)\right) + \epsilon^2\frac{\partial\mu}{\partial z}\frac{\partial w}{\partial r} + 2\epsilon^2\frac{\partial\mu}{\partial r}\frac{\partial u}{\partial r} = 0, \tag{11b}$$
$$-\frac{\partial p}{\partial z} + \epsilon^2\frac{\partial}{\partial z}\left(2\mu\frac{\partial w}{\partial z}\right) + \frac{1}{r}\frac{\partial}{\partial r}\left(\mu r\frac{\partial w}{\partial r}\right) + \frac{\epsilon^2}{r}\frac{\partial}{\partial r}\left(\mu r\frac{\partial u}{\partial z}\right) = 0, \tag{11c}$$
$$\epsilon^2\mathrm{Pe}\left(u\frac{\partial T}{\partial r} + w\frac{\partial T}{\partial z}\right) = \frac{1}{r}\frac{\partial}{\partial r}\left(r\frac{\partial T}{\partial r} + \gamma r\frac{\partial T^4}{\partial r}\right) + \epsilon^2\frac{\partial^2}{\partial z^2}\left(T + \gamma\frac{\partial T^4}{\partial z}\right), \tag{11d}$$

where $\mathrm{Pe} = \hat{\rho}\hat{c}_p\hat{W}_0\hat{L}/\hat{k}_c$ is the Péclet number and $\gamma = 4n_0^2\hat{\sigma}\hat{T}_s^3/3\hat{\chi}\hat{k}_c$ measures the importance of bulk diffusion. The dimensionless boundary conditions are

$$u = \frac{\partial w}{\partial r} = 0 \tag{12a}$$

on $r = 0$ and

$$u = w\frac{\mathrm{d}R}{\mathrm{d}z}, \tag{12b}$$
$$-p + 2\epsilon^2\mu\frac{\partial u}{\partial r} = \epsilon^2\mu\frac{\mathrm{d}R}{\mathrm{d}z}\left(\epsilon^2\frac{\partial u}{\partial z} + \frac{\partial w}{\partial r}\right), \tag{12c}$$
$$\mu\left(\epsilon^2\frac{\partial u}{\partial z} + \frac{\partial w}{\partial r}\right) = \frac{\mathrm{d}R}{\mathrm{d}z}\left(-p + 2\epsilon^2\mu\frac{\partial w}{\partial z}\right), \tag{12d}$$
$$-\left(1 + 4\gamma T^3\right)\frac{\partial T}{\partial r} = \epsilon\alpha\left(T^4 - T_f^4\right) + \epsilon\beta\left(T - T_a\right) \tag{12e}$$

on $r = R(z)$, where $\alpha = \hat{\sigma}\varepsilon_r\hat{T}_s^3\hat{L}/\hat{k}_c$ and $\beta = \hat{k}_h\hat{L}/\hat{k}_c$ represent the importance of conduction relative to radiation and convection respectively. We note that when only one of these effects is accounted for, both α and β have been referred to as the Biot number [9,23]. Typical values are given in Table 2, although these may vary both with the fibre radius and the type of glass used. Finally, we have boundary conditions on the fibre temperature and velocity at input and the pulling speed as the fibre exits the furnace, namely

Table 2 Dimensionless parameter definitions and approximate values

Parameter	Symbol	Approximate value
Aspect ratio	$\epsilon = \hat{R}_0/\hat{L}$	0.1
Reynolds number	$\mathrm{Re} = \dfrac{\hat{\rho}\hat{W}_0\hat{L}}{\hat{\mu}_s}$	$\lesssim 10^{-3}$
Péclet number	$\mathrm{Pe} = \dfrac{\hat{\rho}\hat{c}_p\hat{W}_0\hat{L}}{\hat{k}_c}$	1000
Draw ratio	$w_1 = \dfrac{\hat{W}_1}{\hat{W}_0}$	3×10^4
Surface radiation parameter	$\alpha = \dfrac{\hat{\sigma}\varepsilon_r\hat{T}_s^3\hat{L}}{\hat{k}_c}$	160
Conduction parameter	$\beta = \dfrac{\hat{k}_h\hat{L}}{\hat{k}_c}$	50
Bulk radiation parameter	$\gamma = \dfrac{4n_0^2\hat{\sigma}\hat{T}_s^3}{3\hat{\chi}\hat{k}_c}$	5

$$w(r,0) = 1, \quad T(r,0) = T_0, \quad w(r,1) = w_1, \tag{13f-h}$$

where the draw ratio $w_1 = \hat{W}_1/\hat{W}_0$ is the ratio of axial draw speed to input speed and $T_0 = \hat{T}_0/T_s$ is the dimensionless inlet temperature. Finally, from (3) and taking $a \approx 61000$ K [13] we find the dimensionless viscosity

$$\mu(T) = \exp\left(32(1/T - 1)\right). \tag{14}$$

3 Fluid flow

Seeking regular parameter expansions of the form $u = u^{(0)} + \epsilon^2 u^{(1)} + \cdots$ into the flow problem, (11a–c) and (12a–c), and considering the resulting equations to leading order, we find that $w^{(0)} = w^{(0)}(z)$, and thus the flow is extensional. An approach similar to that of [3] may then be used to derive the following leading-order equations:

$$\frac{\mathrm{d}}{\mathrm{d}z}\left(w^{(0)}R^{(0)2}\right) = 0, \tag{15a}$$

$$\frac{\mathrm{d}}{\mathrm{d}z}\left(3\bar{\mu}^{(0)}R^{(0)2}\frac{\mathrm{d}w^{(0)}}{\mathrm{d}z}\right) = 0, \tag{15b}$$

representing conservation of mass and an axial stress balance respectively, where overbars denote the radially averaged quantity

$$\bar{\phi}(z) = \frac{2}{R^2}\int_0^R r\phi(r,z)\mathrm{d}r. \tag{16}$$

Integrating (15a–b) and applying boundary condition (13f) yields

$$w^{(0)}R^{(0)2} = 1, \tag{17a}$$

$$3\bar{\mu}^{(0)} R^{(0)2} \frac{\mathrm{d}w^{(0)}}{\mathrm{d}z} = F, \tag{17b}$$

where F is the (constant) tension in the fibre. In our problem we prescribe the draw speed $w(1) = w_1$ (chosen here to be 3×10^4, which corresponds to a high draw speed of $30\,\mathrm{ms}^{-1}$). Then F is determined as part of the solution once we have found the temperature and, hence, radially averaged viscosity $\bar{\mu}^{(0)}$ using (14) and (16). We discuss the variation of F with w_1, α and β in §4.1.3.

4 Temperature profiles

The temperature system (11d) and (12e) possesses various asymptotic limits of interest, and we address these in what follows. We note that several of the dimensional parameters given in Table 1, and thus their dimensionless counterparts given in Table 2, are uncertain and may vary by up to an order of magnitude depending on the glass used, and so the different limits will be applicable to these different scenarios.

4.1 Rapid heat transport across fibre radius

4.1.1 Surface radiation and conduction balance axial convection

We begin by supposing that $\mathrm{Pe} = \mathrm{Pe}^*/\epsilon$, where $\mathrm{Pe}^* = O(1)$, and also assume α, β and γ to be of order unity. In practice this corresponds to high conduction, so that it balances both with surface radiation and axial convection. Substituting a regular parameter expansion of the form $T = T^{(0)} + \epsilon T^{(1)} + \cdots$ into (11d) and using (12e) indicates that $T^{(0)} = T^{(0)}(z)$, and thus there are no variations in temperature across the fibre. The system is closed by proceeding to second order in (11d), integrating over the fibre radius and using (12e) and (17a), leading to the system

$$3\bar{\mu}^{(0)}(T^{(0)}) \frac{\mathrm{d}w^{(0)}}{\mathrm{d}z} = F w^{(0)}, \tag{18a}$$

$$\frac{1}{2}\sqrt{w^{(0)}}\mathrm{Pe}^* \frac{\mathrm{d}T^{(0)}}{\mathrm{d}z} = -\left(\alpha\left(T^{(0)4} - T_\mathrm{f}^4\right) + \beta\left(T^{(0)} - T_\mathrm{a}\right)\right), \tag{18b}$$

subject to boundary conditions

$$w^{(0)}(r, 0) = 1, \quad T^{(0)}(r, 0) = T_0, \quad w^{(0)}(r, 1) = w_1. \tag{19a-c}$$

The evolution of temperature, viscosity, axial velocity and radius with axial position, taking the illustrative parameter choice $\mathrm{Pe}^* = 1$, for different (but constant in space) values of α and β is shown in Fig. 2, where we have assumed the Gaussian furnace temperature profile (9). We see that the viscosity varies through many orders of magnitude as the fibre is drawn through the furnace. The fibre temperature is heavily guided by the furnace temperature, peaking around or just after the furnace peak temperature. Following this, the temperature then falls throughout the remainder of the furnace. The axial velocity and fibre radius both vary over a relatively small axial distance, corresponding to the region where the glass temperature is near its maximum.

We notice that the axial velocity of the glass dramatically increases as we move down the profile. As a result it is useful to visualize the temperature profile of a material element of molten glass as it moves through the furnace. This corresponds to determining the temperature as a function of a dimensionless 'time variable', $\tau = \tau(z)$, defined by

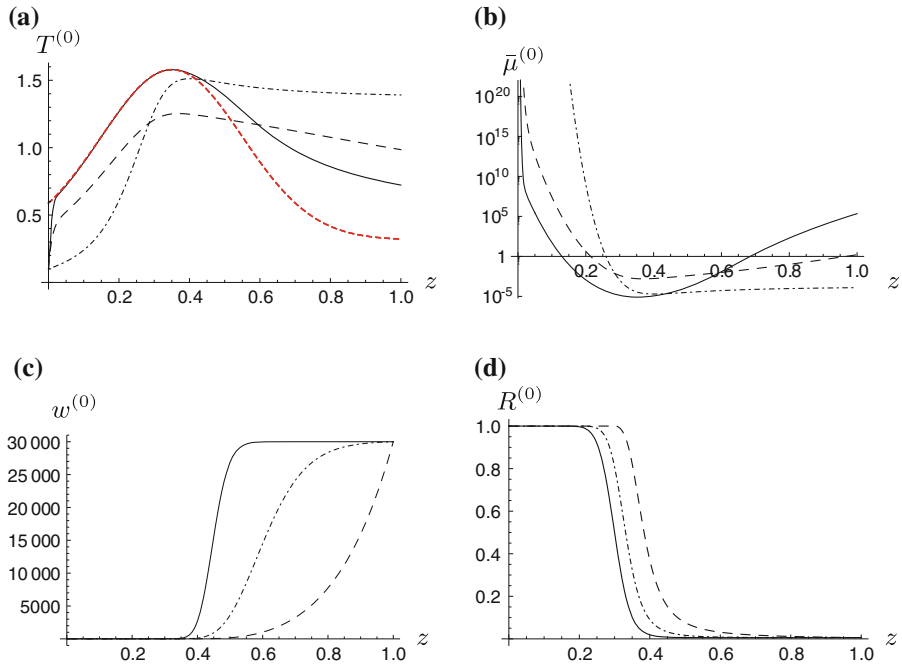

Fig. 2 Effect of varying furnace temperature on leading-order variation of **a** temperature, **b** viscosity, **c** axial velocity and **d** radius, with axial position for $\mathrm{Pe}^* = 1$, $w_1 = 3 \times 10^4$, $T_\mathrm{a} = 3T_\mathrm{f}/4$, $T_0 = T_\mathrm{s}/10$. In all cases the *black solid line* illustrates the case where $\alpha = 160$, $\beta = 1$, the *dotted–dashed line* shows the case $\alpha = 1$, $\beta = 50$, and the *dashed line* shows the case $\alpha = 1$, $\beta = 1$. The *red dashed line* in **a** shows the furnace temperature $T_\mathrm{f}(z)$, given by (9) with $T_\mathrm{m} = 3000\,\mathrm{K}$. (Color figure online)

$$\tau = \int_0^z \frac{1}{w^{(0)}(\zeta)}\,\mathrm{d}\zeta, \tag{20}$$

which we identify with the time at which an element starting at the top of the furnace reaches the axial position z. The rapid acceleration of the glass as it moves towards the end of the furnace is clearly shown by the relation between τ and axial position z in Fig. 3a. The rapid cooling is evident in Fig. 3b–d, where we show the temperature, viscosity and fibre radius varying dramatically in the final stages of the drawing process.

Aside from exhibiting all of the general features that are found in practice, these examples also illustrate the effect of α and β on the process: a higher β leads to stronger cooling, whereas a higher α is needed to raise the glass temperature to the furnace temperature. To examine this more closely, we consider the case of a constant furnace temperature T_f in Fig. 4.[2] These plots clearly illustrate the initial boundary layer in which the glass temperature rapidly increases from T_0 to its equilibrium value T_e given by the solution to

$$\alpha\left(T_\mathrm{e}^4 - T_\mathrm{f}^4\right) + \beta\left(T_\mathrm{e} - T_\mathrm{a}\right) = 0. \tag{21}$$

Furthermore, we see that the boundary layer width decreases with increasing α, while changing β affects only the steady-state value attained. For the large values of α typically observed in practice, we are therefore justified in ignoring this initial transient and setting $T_0 = T_\mathrm{e}$ as the initial condition for the temperature.

[2] The constant T_f case is amenable to phase-plane analysis, details of which may be found in the appendix.

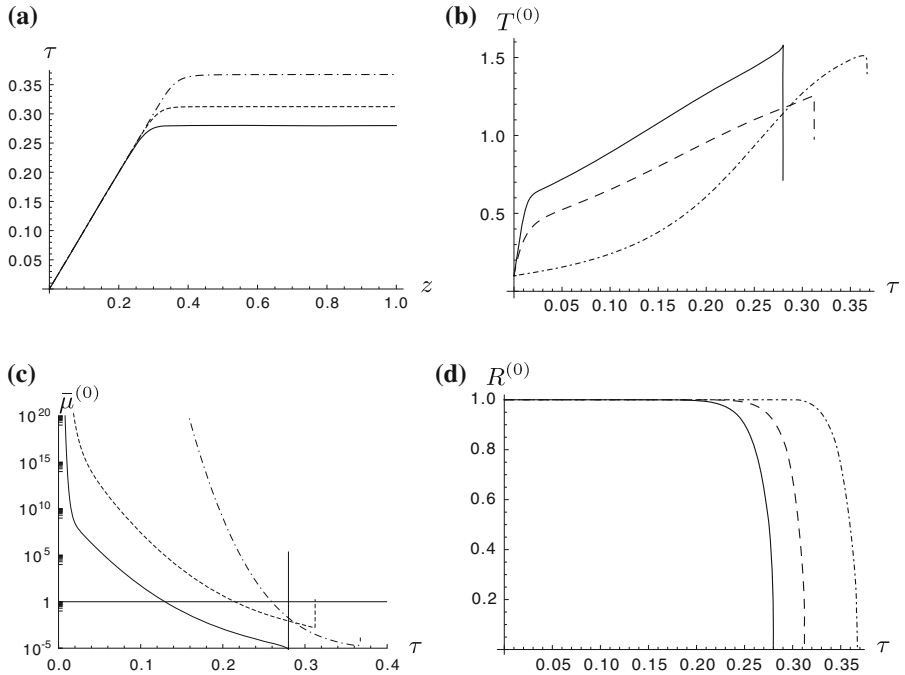

Fig. 3 **a** Time variable τ against axial distance z for $\alpha = 160$, $\beta = 1$ (*solid line*), $\alpha = 1$, $\beta = 50$, (*dotted–dashed line*) and $\alpha = 1$, $\beta = 1$ (*dashed line*). The corresponding **b** temperature, **c** viscosity and **d** radius are plotted against τ. In all cases $\mathrm{Pe}^* = 1$, $w_1 = 3 \times 10^4$, $T_\mathrm{a} = 3T_\mathrm{f}/4$, $T_0 = T_\mathrm{s}/10$

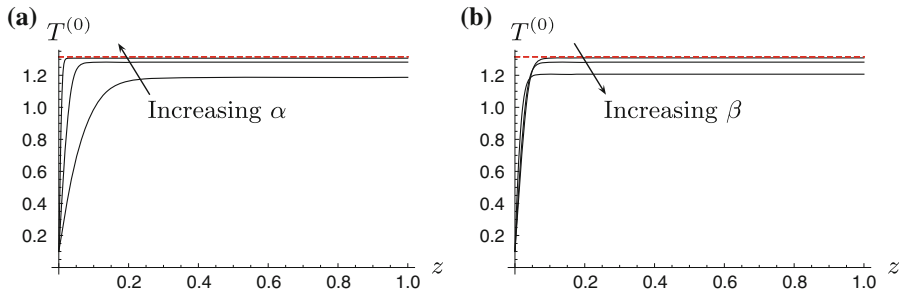

Fig. 4 Influence of **a** α and **b** β on variation of glass temperature with axial position taking a constant furnace temperature $T_\mathrm{f} = 2500\,\mathrm{K}$, shown *red* (*dashed*). In **a** we take $\beta = 5$, $\alpha = \{1, 5, 20\}$, whereas in **b** $\alpha = 1$, $\beta = \{1, 5, 20\}$. In all cases $\mathrm{Pe}^* = 1$, $w_1 = 3 \times 10^4$, $T_\mathrm{a} = 3T_\mathrm{f}/4$, $T_0 = T_\mathrm{s}/10$. (Color figure online)

4.1.2 Effect of $\alpha(z)$, $\beta(z)$

We now consider the effect of letting α and β vary in the axial direction. Following our discussion in § 2.1.5, we take $\varepsilon_\mathrm{r} \sim 1 - \mathrm{e}^{-\phi\hat{R}}$ with $\phi = 2.5\hat{\chi}$ and use (17a) to obtain

$$\alpha(z) = \alpha_0 \left(1 - \mathrm{e}^{-25/\sqrt{w^{(0)}(z)}}\right), \tag{22a}$$

where α_0 is a constant. Taking $\hat{R}\hat{k}_\mathrm{h} \sim (\hat{w}\hat{R})^{1/3}$ as discussed in § 2.1.5 and using (17a) leads to

$$\beta(z) = \beta_0 {w^{(0)}}^{2/3}, \tag{22b}$$

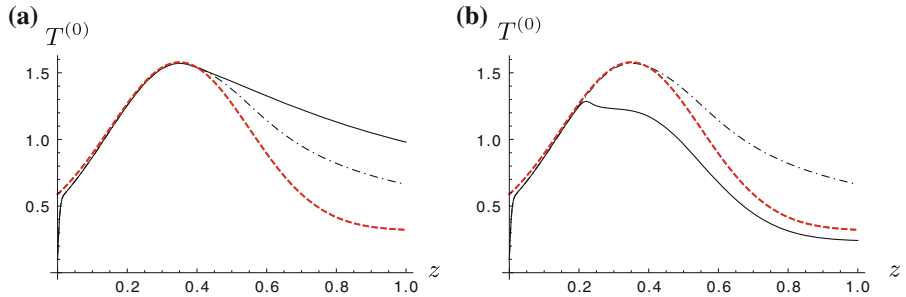

Fig. 5 Influence of **a** $\alpha(z)$ given by Eq. (22a) (*solid curve*) and **b** $\beta(z)$ given by Eq. (22b) (*solid curve*), compared to constant values $\alpha_0 = 160$ and $\beta_0 = 50$ (*dotted–dashed*); the furnace temperature is also shown (*dashed*). In all cases $\mathrm{Pe}^* = 1$, $w_1 = 3 \times 10^4$, $T_\mathrm{a} = 3T_\mathrm{f}/4$, $T_0 = T_\mathrm{s}/10$

where β_0 is a constant.

We compare the difference between constant α and $\alpha(z)$ (with β held constant) in Fig. 5a, where we see that a lower glass temperature is taken on exiting the furnace when α is a constant than when α varies with axial position. When α depends upon the axial position, Newton cooling is the dominant mechanism in the later stages of the process, as argued by, for example, [9]. Data for the exit glass fibre temperature would provide a mechanism to determine the most suitable form for α.

On the other hand, we see in Fig. 5b that, with the proposed functional form for $\beta(z)$, the temperature drops off before the furnace reaches its maximum temperature and the glass viscosity is not reduced enough to enable effective drawing. We therefore believe that this form is not realistic and that β should be kept constant. This is in agreement with the numerical results to the full conjugate heat transfer problem, which reported that $\hat{k}_\mathrm{h}$ remained approximately constant throughout the process [25].

For the remainder of this paper we focus our attention on the case where α and β are constant.

4.1.3 The force

An important quantity for industrial applications is the force, F, required to draw a fibre, found as part of the solution to (18), satisfying $F = 3 \log w_1 / \int_0^1 1/\bar{\mu}^{(0)} \mathrm{d}z$. We plot the force as a function of the prescribed draw ratio w_1 in Fig. 6a, which, as expected, is a monotonically increasing function. We also plot the force against α and β in Figs. 6b and c; interestingly, the former is found to be non-monotonic at low values of α.

We note that, for a rapidly varying choice of $\mu(T)$, Wylie et al. [23] reported that a simplified model with constant heating and no cooling could predict three possible branches in force/draw-ratio space, two of which were potentially stable. This surprising result was later extended to include surface tension and inertial effects [20]. Although we have also been able to reproduce their results for our model using the $\mu(T)$ form suggested by Wylie et al. [23], the solutions are very sensitive to the parameter values; in particular, we have not found the three branches for our choice of $\mu(T)$ and range of realistic parameter values.

4.1.4 Surface radiation and conduction dominate

Our parameter estimates given in Table 1 suggest that both α and β may in fact be quite large. If we therefore assume that $\alpha = \lambda\alpha^*$ and $\beta = \lambda\beta^*$, where α^*, β^* are of order unity and $\lambda \gg 1$, then surface radiation and conduction dominates over axial convection, and we may neglect the left-hand side of (18b). If we now assume that α^* and β^* are constant, then $T^{(0)}(z)$ is given simply by $\mathcal{T}(z)$, the solution to the quartic equation

$$\alpha^* \left(\mathcal{T}(z)^4 - T_\mathrm{f}(z)^4 \right) + \beta^* \left(\mathcal{T}(z) - T_\mathrm{a}(z) \right) = 0, \tag{23}$$

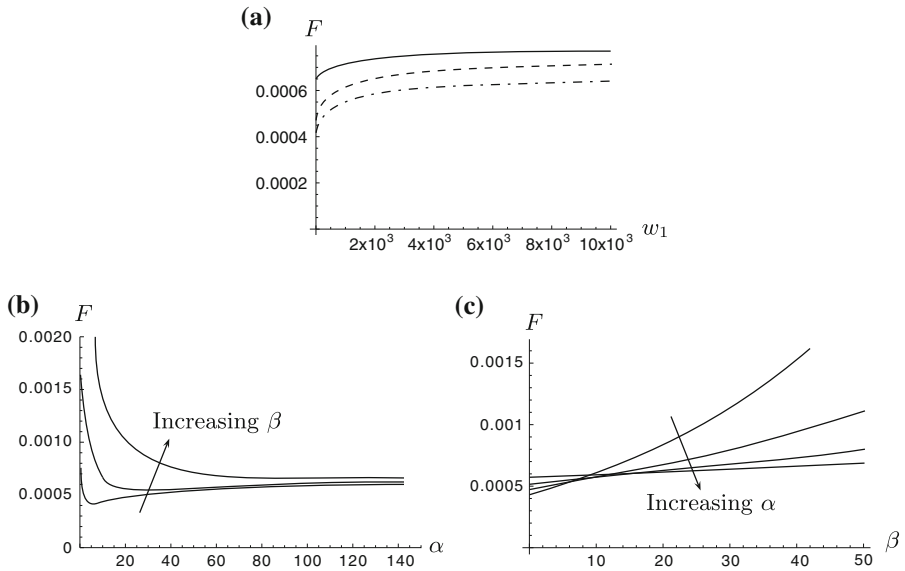

Fig. 6 Force F against **a** w_1 for $\alpha = 160$, $\beta = 50$ (*solid*), $\alpha = 1$, $\beta = 50$ (*dashed*), $\alpha = 1$, $\beta = 1$ (*dotted–dashed*), **b** α for $\beta = \{1, 10, 50\}$, $w_1 = 3 \times 10^4$, **c** β for $\alpha = \{10, 20, 50, 100\}$, $w_1 = 3 \times 10^4$. In all cases, $\mathrm{Pe}^* = 1$, $T_\mathrm{a} = 3T_\mathrm{f}/4$, $T_0 = T_\mathrm{s}/10$

which may be expressed explicitly, although, due to its complicated form, we refrain from writing it here. Once determined, (18a) may be integrated to give

$$w^{(0)} = \exp\left(\int_0^z \frac{3F}{\bar{\mu}^{(0)}(T(s))}\mathrm{d}s\right), \tag{24}$$

with F chosen such that $w^{(0)}(1) = w_1$, and $R^{(0)}$ may then be calculated from (17a).

Towards the end of the furnace the fibre velocity rises significantly, and the term neglected on the left-hand side of (18b) becomes important again; a boundary layer is thus present. Rescaling $w^{(0)} = \lambda^2 \mathcal{W}$ we find that system (18b) now reads

$$\frac{1}{2}\sqrt{\mathcal{W}}\mathrm{Pe}^*\frac{\mathrm{d}T^{(0)}}{\mathrm{d}z} = -\left(\alpha^*\left(T^{(0)^4} - T_\mathrm{f}^4\right) + \beta^*\left(T^{(0)} - T_\mathrm{a}\right)\right), \tag{25}$$

and we return to solving the original full system (18). However, since the numerical simulations indicate that the velocity evolves to its final value over a fairly narrow window (near where the temperature attains its maximum), its value is approximately constant (and equal to the draw speed) for an appreciable portion of the fibre drawing. We thus propose that we may set $\mathcal{W}_1 = W_1/\lambda^2 (= O(1))$, the (known) fibre pulling speed, so that (25) provides a decoupled autonomous equation for $T^{(0)}$ in this region, which may be solved implicitly to give

$$z\left(T^{(0)}\right) = -\int_1^{T^{(0)}} \frac{\sqrt{W_1}\mathrm{Pe}^*\,\mathrm{d}s}{\alpha^*\left(s^4 - T_\mathrm{f}^4\right) + \beta^*(s - T_\mathrm{a})}. \tag{26}$$

We may then patch the solution to (23) with the solution to (26) to find an approximation to the full temperature distribution. Once determined, $w^{(0)}$ and $R^{(0)}$ are easily calculated from (18a) and (17a) as before. This patched asymptotic solution is compared with the solution to the full coupled system (18) in Fig. 7, showing excellent

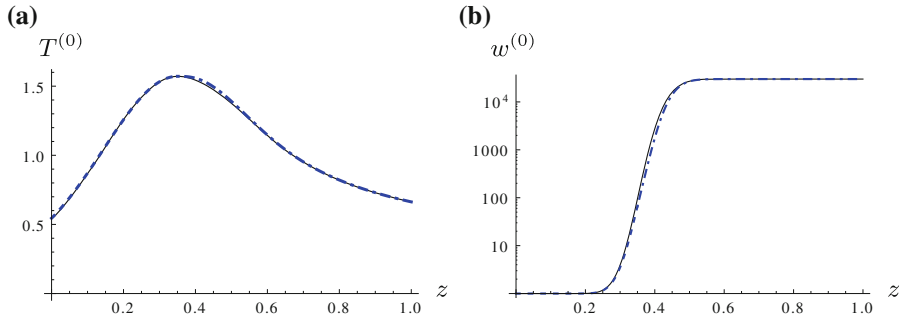

Fig. 7 **a** Variation of leading-order temperature with axial position given by full system (18) when $\mathrm{Pe} = 1$, $\alpha = 160$ and $\beta = 50$ (*black*), while the *blue dashed line* shows the asymptotic solution $\mathcal{T}$ given by (23). In both cases, $\mathrm{Pe}^* = 1$, $w_1 = 3 \times 10^4$, $T_\mathrm{a} = 3T_\mathrm{f}/4$, $T_0 = T_\mathrm{e}$. In (**b**), the corresponding numerical and asymptotic solutions for the fibre radius are shown. (Color figure online)

agreement, with the two solutions almost indistinguishable. To complete a formal asymptotic analysis, we need to solve the full problem in a small region that matches the solution determined in the two regions here. Nevertheless, the asymptotic solutions derived here provide a simple yet accurate description of the system behaviour.

4.1.5 First-order correction

The α, β limit discussed in §4.1.4 may be treated in an asymptotically rigorous manner by setting $\alpha = \alpha^*/\epsilon^p$, $\beta = \beta^*/\epsilon^q$, where $p, q \in \mathbb{Z}_+$. Since the leading-order system depends only on the axial position, to quantify the radial variations, we must analyse the system at the next order in the expansion in powers of ϵ. In doing so, provided $w^{(0)}$ is of order unity, which we have seen is true up to the point where the glass reaches its maximum temperature, we may use Eq. (11d) and boundary condition (12e) at $O(\epsilon)$ (recalling that $\epsilon\mathrm{Pe} = \mathrm{Pe}^*$) to obtain

$$T(r,z) = \mathcal{T}(z) + \epsilon\left[\frac{\mathrm{Pe}^*(r^2 - {R^{(0)}}^2)w^{(0)}\mathcal{T}'(z)}{4(1+4\gamma\mathcal{T}(z)^3)} + A(z)\right]. \tag{27}$$

Here, $A(z)$ depends on the size of p and q: provided α^* and β^* are kept constant, we find from (12e) that

$$A(z) = \begin{cases} -\dfrac{\mathrm{Pe}^* w^{(0)}\mathcal{T}'(z)R}{2(\beta^* + 4\alpha^*\mathcal{T}(z)^3)} & p = q = 1, \\ -\dfrac{\beta^*}{\alpha^*}\dfrac{(T_\mathrm{f} - T_\mathrm{a})}{4T_\mathrm{f}^3} & p = 2, q = 1, \\ -\dfrac{\alpha^*}{\beta^*}\dfrac{1}{(T_\mathrm{a}^4 - T_\mathrm{f}^4)} & p = 1, q = 2, \\ 0 & p, q \geq 2. \end{cases} \tag{28}$$

We plot the temperature profile (27) against both the axial position and scaled radial position, $x(r,z) = r/R^{(0)}(z)$, for the case $p = 2$, $q = 1$ in Fig. 8, showing excellent agreement with the numerical solution to the full two-dimensional problem (§4.2), at least until the temperature reaches its maximum. After this point the axial velocity $w^{(0)}$ increases rapidly and we can no longer ignore the left-hand side of (11d). Nevertheless, these asymptotic results give us a useful check on our two-dimensional numerical solution, which we now discuss.

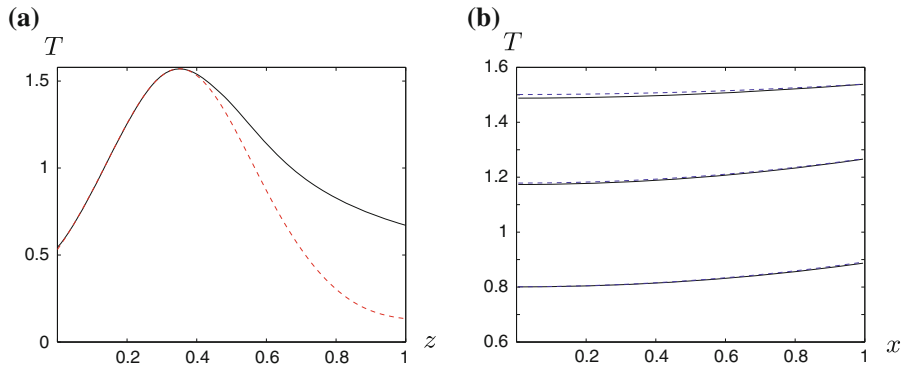

Fig. 8 Numerical (*solid*) and asymptotic (*dashed*) results for temperature against **a** axial position, with $x = 0$, and **b** scaled radial position, x, with $z = \{0.1, 0.2, 0.3\}$, taking $\epsilon = 0.1$, $\mathrm{Pe}^* = 1$, $\alpha = 1.6/\epsilon^2$, $\beta = 5/\epsilon$, $\gamma = 0$, $w_1 = 3 \times 10^4$, $T_\mathrm{a} = 3T_\mathrm{f}/4$, and $T_0 = T_\mathrm{e}$

4.2 Transport across the fibre balancing convection

4.2.1 Surface radiation and conduction balance convection

We now let $\mathrm{Pe} = O(1/\epsilon^2) = \mathcal{P}/\epsilon^2$, which is likely to be relevant to fibre drawing at the higher speeds that have become possible more recently [25]. In this case, heat transfer across the fibre is balanced by the convective transport and, from (11d), we see that $T^{(0)}$ depends on both r and z. However, it is convenient to change variables into a coordinate frame that adapts to the radius of the fibre, via

$$x(r, z) = \frac{r}{R^{(0)}(z)}, \quad \zeta = \mathcal{P}\, z. \tag{29}$$

This transforms system (11d) and (12e) into

$$\frac{\partial T^{(0)}}{\partial \zeta} = \frac{1}{x}\frac{\partial}{\partial x}\left[x\frac{\partial T^{(0)}}{\partial x}\left(1 + 4\gamma {T^{(0)}}^3\right)\right], \tag{30a}$$

with

$$-\frac{\partial T^{(0)}}{\partial x}\left(1 + 4\gamma {T^{(0)}}^3\right) = \alpha^* R^{(0)}\left({T^{(0)}}^4 - T_\mathrm{f}^4\right) + \beta^* R^{(0)}\left(T^{(0)} - T_\mathrm{a}\right) \tag{30b}$$

on $x = 1$, where we have set $\alpha = \alpha^*/\epsilon$ and $\beta = \beta^*/\epsilon$, as this provides the richest limit in which surface radiation and conduction balance convection.

In general, we must solve (30) numerically together with (17). We discretize the differential equations using second-order centred differences for the spatial derivatives and integrate in time using the MATLAB differential-algebraic equation solver `ode15s`, treating (17b) as an algebraic constraint at each time-step. Once the solution is found for an initial guess for F, the process is repeated iteratively until boundary condition (13h) is satisfied at the end of the domain.

4.2.2 Industrially relevant regime

Based on the parameter values given in Table 1, we take $\alpha^* = 16$, $\beta^* = 5$, $\gamma = 5$ and consider the effect of the Péclet number, which is directly proportional to the preform width W_0 and, thus, the draw ratio; indeed Péclet numbers

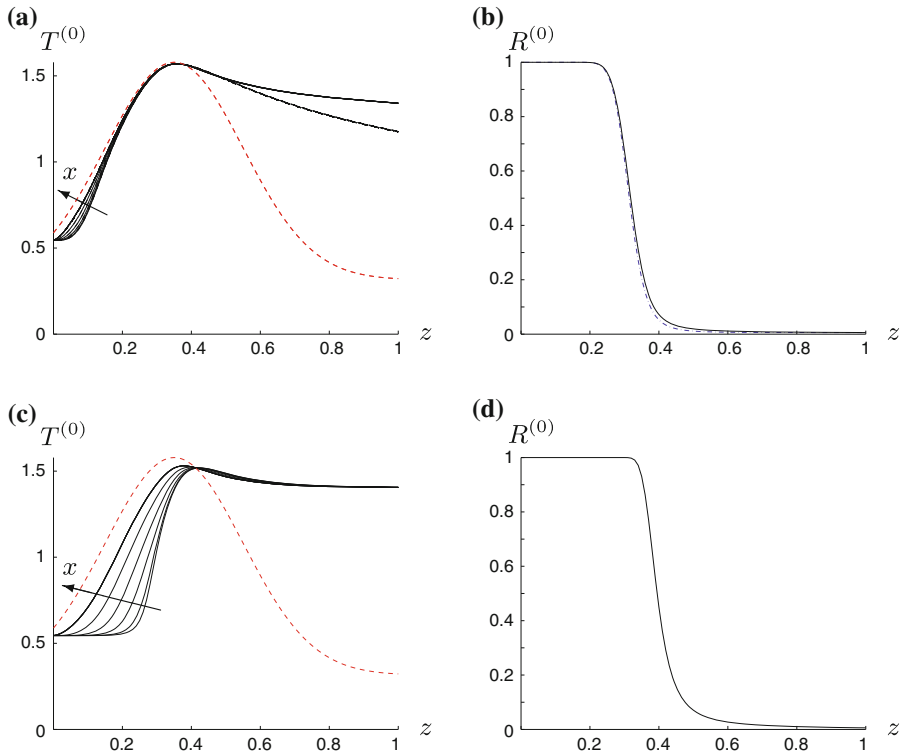

Fig. 9 **a** Variation in leading-order temperature with axial position for radial coordinate $x = \{0, 0.2, 0.4, 0.6, 0.8, 1\}$ in the case **a** $\mathcal{P} = 1$ and **c** $\mathcal{P} = 10$; the furnace temperature is also shown (*dashed*). **b, d** Corresponding fibre radii. In all cases, $\alpha = 16/\epsilon$, $\beta = 5/\epsilon$, $\gamma = 5$, $w_1 = 3 \times 10^4$, $T_a = 3T_f/4$ and $T_0 = T_e$, whereas in **a** and **c**, we also show the case of $\alpha(z)$ using (22a) (*dot-dashed*)

as high as $O(10^3)$ are possible in high-speed fibre drawing. We present numerical results for the temperature and free-surface profiles for $\mathcal{P} = 1, 10$ in Fig. 9 (for ease of comparison we have used z rather than the rescaled variable ζ). As expected, we see that the temperature now varies across the radius of the fibre, being hottest at the edge and coolest in the middle. Furthermore, this variation is much more pronounced at the larger Péclet number, as suggested from the rescaling (29).

Although we are able to solve the full system numerically, we note that in the limit of strong radiation (as suggested by our parameter values) or strong cooling, Eqs. (30a) and (30b) de-couple, which leads to a simplified system. For example, setting $\alpha = \hat{\alpha}/\epsilon^2$ and $\beta = \hat{\beta}/\epsilon^2$, where $\hat{\alpha}$ and $\hat{\beta}$ are $O(1)$, the leading-order boundary condition (30b) simplifies to $T^{(0)} = \mathcal{T}(\zeta)$ on $x = 1$, where $\mathcal{T}$ is again given by (23) with α^*, β^* replaced by $\hat{\alpha}$, $\hat{\beta}$ respectively.

4.2.3 Effect of bulk radiation

We now consider the role of bulk radiation, which for $\mathrm{Pe} = O(1/\epsilon^2)$ comes in at leading order when $\gamma = O(1)$, as assumed thus far. From (30) we see that if $\gamma \gg 1$, then bulk radiation dominates, so that the temperature is approximately constant across the fibre. On the other hand, if we now set $\gamma = 0$, that is, zero bulk radiation, the model reduces to

$$\frac{\partial T^{(0)}}{\partial \zeta} = \frac{1}{x}\frac{\partial}{\partial x}\left(x\frac{\partial T^{(0)}}{\partial x}\right) \quad \text{in } 0 < x < 1, \tag{31a}$$

$$T^{(0)} = \mathcal{T}(\zeta) \quad \text{at } x = 1, \tag{31b}$$

$$T^{(0)} \text{ bounded} \quad \text{at } x = 0, \tag{31c}$$

$$T^{(0)} = \mathcal{T}(0) \quad \text{at } \zeta = 0, \tag{31d}$$

and in this case we are able to solve explicitly for the temperature. We let $T^{(0)}(x, \zeta) = \mathcal{T}(\zeta) + \hat{T}(x, \zeta)$ and pose the ansatz[3] that

$$\hat{T}(x, \zeta) = \sum_{m=1}^{\infty} f_m(\zeta) J_0(\lambda_m x), \tag{32}$$

where J_0 is the lowest-order Bessel function and λ_m are the roots of J_0. We substitute (32) into (31a), multiply by $x J_0(\lambda_n x)$ and integrate across the fibre to find that f_m satisfies

$$f_m' + \lambda_m^2 f_m = -\frac{2\mathcal{T}'}{\lambda_m J_1(\lambda_m)}, \tag{33}$$

where J_1 is the first-order Bessel function and the solution for f_m is given by

$$f_m = -\frac{2\mathrm{e}^{-\lambda_m^2 \zeta}}{\lambda_m J_1(\lambda_m)} \int_0^{\zeta} \mathcal{T}'(s) \mathrm{e}^{-\lambda_m^2 s} \mathrm{d}s, \tag{34}$$

and so the solution for $T^{(0)}$ is

$$T^{(0)}(x, \zeta) = \mathcal{T}(\zeta) + \sum_{m=1}^{\infty} -\frac{2J_0(\lambda_m x)\mathrm{e}^{-\lambda_m^2 \zeta}}{\lambda_m J_1(\lambda_m)} \int_0^{\zeta} \mathcal{T}'(s) \mathrm{e}^{-\lambda_m^2 s} \mathrm{d}s. \tag{35}$$

We plot the expression for $T^{(0)}$ given by (35), using ten terms in the summation, in Fig. 10a, where we see excellent agreement with numerical results everywhere except near the origin, where the modulus of the terms in the expansion start becoming very large, leading to numerical errors. Once we have found the temperature, we may now calculate $\bar{\mu}$ and use (17) to find $w^{(0)}$, $R^{(0)}$ and F. The corresponding fibre radius is shown in Fig. 10b. In addition to giving a simple explicit solution, (35) also provides a validation for the full two-dimensional numerics.

We compare our solution for zero bulk radiation to one with non-zero bulk radiation, but all other parameters kept constant, in Fig. 10c and d. As expected, with zero bulk radiation we find a greater variation in temperature across the fibre, which leads to a greater radially averaged glass viscosity, so that a greater force is required to pull the fibre through the furnace. Increasing γ aids the heat transfer through the filament cross section and hence smooths the temperature out across the fibre.

5 Discussion

In this paper we derived and analysed an extensional-flow model to describe the evolution of an optical fibre with axial position drawn at high speed, in which we track the radius of the fibre, the speed of the fibre and the temperature.

[3] We choose this particular form by analogy with the solution to the case where $\mathcal{T}(\zeta) = \mathcal{T}$ (a constant), where it is clear that the solution is of the form $T^{(0)}(x, \zeta) = \mathcal{T} + \sum_{m=1}^{\infty} f_m(\zeta) J_0(\lambda_m x)$, with a simpler form for f_m.

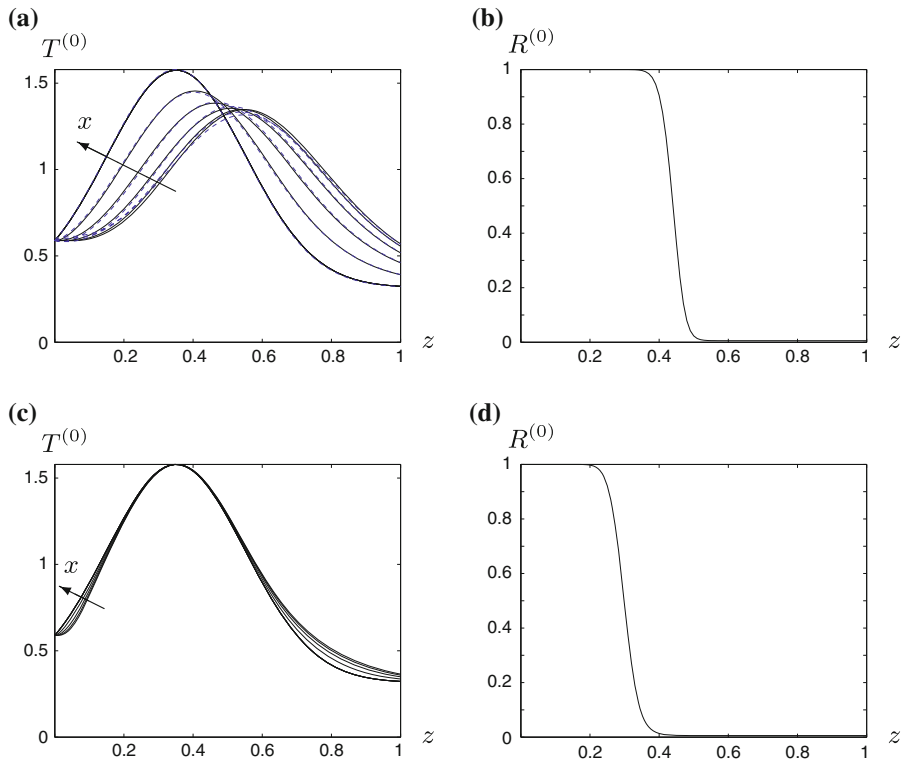

Fig. 10 **a** Variation in leading-order temperature with axial position for $x = \{0, 0.2, 0.4, 0.6, 0.8, 1\}$ in the case $\mathcal{P} = 1$, $\hat{\alpha} = 1$, $\hat{\beta} = \gamma = 0$. The *solid lines* correspond with the numerical solution of (31a), whereas the *dashed lines* correspond to the exact solution (35) taking ten terms in the expansion. The corresponding fibre radius is shown in (**b**). **c** and **d** are the same as **a** and **b**, except $\gamma = 5$

We incorporated energy transfer due to conduction, convection, bulk and surface radiation, and convective cooling from the air, assuming that the fibre was optically thick. We also included the dependence of the viscosity on temperature.

The model was first solved numerically in the limit where the temperature did not vary across the fibre. A change of variable allowed us to present the solutions in terms of a Lagrangian time variable that traces a material fluid element as it passes down the fibre. In terms of this variable, a boundary layer near the end of the evolution was shown to exist. The structure of this solution was determined in the original coordinate system using asymptotic analysis. The domain decomposed into an initial region where the temperature was set by a balance between surface radiation and convective cooling, in which the velocity and fibre radius varied significantly, and then a later region where the radius and velocity were effectively constant and the evolution of the temperature also involved bulk convection.

Other interesting parameter limits of the model were explored using asymptotics and numerics. In an industrially relevant limit, the temperature varies along and across the fibre, but the qualitative features are the same as in the radially invariant case. The model can be used to assess the relative importance of surface cooling, surface radiation, bulk radiation and standard heat transfer on the evolution of a fibre. In particular, including bulk radiation smooths the temperature profile across the fibre, as shown in Fig. 10.

Our analysis has always assumed a known (large) pulling speed, with the required force calculated as part of the solution. As expected, this force increases monotonically with the pulling speed and also increases as the glass viscosity decreases, for example when the Péclet number is particularly high, as investigated in § 4.2.2. In fact, we note that there *always* exists a force F that allows us to solve our one- or two-dimensional model, although it may be unfeasibly high for practical purposes. This is in contrast to the more elaborate two- and three-dimensional models

of Jaluria and co-workers, who are unable to find a steady solution if the glass temperature is too low, suggesting that the fibre solidifies and breaks.

Throughout this paper we have restricted ourselves to considering only steady profiles, yet it has long been known that even for an isothermal fibre draw ratio the problem becomes unstable once the draw ratio exceeds a critical value $w_{\text{crit}} \approx 20$ [10]. This oscillatory instability is known as *draw resonance* and is of both mathematical interest [16] and great practical importance. A number of authors have thus investigated both the linear [8,13] and nonlinear [6] stability of non-isothermal fibre drawing. While it would be possible to follow the same methodology for our model, we note that [19] recently performed an in-depth study on the effect of cooling on fibre drawing, noting that it is governed by the Stanton number $St = \beta/\epsilon\text{Pe}$. Provided this is not much greater than unity, as found from our parameter estimates, cooling has a stabilizing effect on fibre drawing, which would aid the process.

As discussed in §2.1, a limitation in our model is the assumption of an optically thick fibre, which is likely to break down once the fibre is at its thinnest. Unfortunately, determining the energy transfer for an optically thin fibre would involve tracing rays within the fibre; methods to do so have been discussed by, for example, [11,12] and, more recently, [7]. Secondly, we should solve for the temperature field outside the fibre, taking into account that the convective transfer to the fibre will be affected by the speed of the fibre and that the presence of the air will affect the (external) radiative transfer.

However, the foregoing extensions would necessarily involve computationally intense problems, negating the entire philosophy behind our work, that is, to derive realistic yet simple models for fibre drawing that may be solved quickly. In light of this, useful extensions to our models that could still be readily solved would be the inclusion of multiple layers, as discussed by [2,21], and of viscous dissipation. This latter effect was analysed for a simplified case by [22], who found that dissipative effects were important once the fibre had thinned, and a one-dimensional analysis required the inclusion of inertial effects. Similarly, [11] argued that viscous dissipation made two-dimensional effects important, and so it would be expedient to include this effect in future extensions of our work.

Acknowledgments This paper was conceived as an extension to a problem considered at the 27th Annual Workshop on Mathematical Problems in Industry held at the New Jersey Institute of Technology in June 2011, with funding from the National Science Foundation. We would like to thank A. Filippov from Corning Inc., who presented the problem at the workshop and gave us invaluable insight into the practical issues involved. We would also like to thank the other participants who worked on different aspects of the problem: R. Beckham, M. Gratton, M. Kanoria, K. Kilgore, V. Lapin, T-S. Lin, M. Ma, H. Nganguia, J. Pohlmeyer, H. Potter, D. Schwendeman, S. K. Wilson, and H. Yaple. Finally, the authors note that this publication was based on work supported in part by Award No. KUK-C1-013-04, made by King Abdullah University of Science and Technology (KAUST).

Appendix

Phase plane analysis at constant furnace temperature

As noted in the main text, system (18a,b) is amenable to a phase plane analysis in the case where the furnace temperature T_{f} is assumed constant (for consistency with the assumption of §2.1.4 the ambient temperature T_{a} is then also constant). Dropping all leading-order $^{(0)}$ superscripts to simplify notation, it proves convenient to consider the phase plane in (w, μ)-space. With $T(\mu)$ given by inverting relation (14), the autonomous system (18a,b) then becomes

$$\frac{\mathrm{d}w}{\mathrm{d}z} = \frac{Fw}{3\mu}, \tag{36}$$

$$\frac{\mathrm{d}\mu}{\mathrm{d}z} = \frac{64\mu}{\text{Pe}^* T(\mu)^2\sqrt{w}}\left(\alpha(T(\mu)^4 - T_{\text{f}}^4) + \beta(T(\mu) - T_{\text{a}})\right), \tag{37}$$

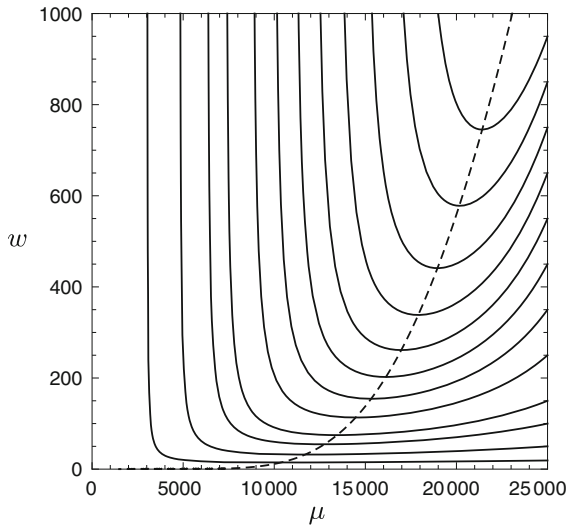

Fig. 11 Phase plane for ambient temperature below glass-cooling temperature. If the draw ratio is sufficiently high, then the fibre viscosity may increase again before the fibre exits the furnace

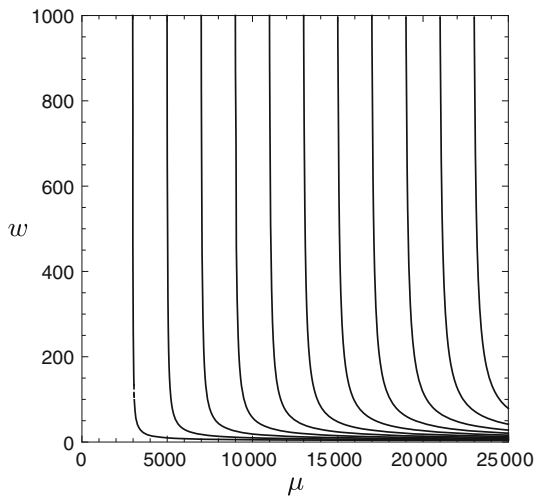

Fig. 12 Phase plane for ambient temperature above glass-softening temperature. The fibre viscosity decreases monotonically as the fibre passes through the furnace for all draw ratios

with $T(\mu) = (1 + \log(\mu)/32)^{-1}$. The phase plane for this system is the solution trajectories of the ordinary differential equation

$$\frac{\mathrm{d}w}{\mathrm{d}\mu} = \frac{\mathrm{Pe}^* F T(\mu)^2 w^{3/2}}{192\mu^2 \left(\alpha(T(\mu)^4 - T_\mathrm{f}^4) + \beta(T(\mu) - T_\mathrm{a})\right)}. \tag{38}$$

As in the main text, we can consider either constant α, β, or $\alpha(w)$, $\beta(w)$ as in, for example, Eq. (22). Here we present two representative example phase planes for the case in which α and β are functions of w. A key factor influencing the qualitative features of the phase diagram is whether the ambient temperature T_a is greater than or less than the glass-softening temperature. In Fig. 11 we show the phase plane for $\alpha = \alpha_0(1-\exp(-10/\sqrt{w}))$, $\beta = \beta_0 w^{2/3}$, and with $\alpha_0 = 160$, $\beta_0 = 1$, $T_\mathrm{f} = 1.57$, $T_\mathrm{a} = 0.75$ (lower than the glass-softening temperature, which normalizes to 1), and $\mathrm{Pe}^* F = 3840$. The solid curves are the phase trajectories, while the dashed curve is the nullcline on which $\alpha(T(\mu)^4 - T_\mathrm{f}^4) + \beta(T(\mu) - T_\mathrm{a}) = 0$. Only a limited range of the μ-axis is shown for simplicity, but it is clear what the evolution would be for such a fibre. The fibre enters at a small value of w, the input velocity. At this stage its viscosity is extremely large. As the fibre enters further into the furnace it gains axial velocity and its viscosity drops precipitously before levelling off. Depending on the draw ratio (ratio of exit velocity to input velocity), the viscosity may reach a minimum value (phase path crossing a nullcline) and then increase again before the fibre exits the furnace.

In the case where the ambient temperature T_a is higher than the softening temperature, the evolution is less dramatic. An example is shown in Fig. 12, with all parameters as before except $T_\mathrm{a} = 1.18 > 1$. In this case, the viscosity again drops rapidly as the fibre enters the furnace, but then stays at a low value until exit.

Bearing in mind the comments of §4.1.2 about the unrealistic nature of the proposed functional dependence of β, we also show a phase plane for the case of constant $\beta = 50$ (Fig. 13). In this case the phase plane shows no qualitative difference between the cases where the ambient temperature is above or below the softening temperature, so we show only the case considered throughout most of the paper, where $T_\mathrm{a} = 3T_\mathrm{f}/4 = 1.18 > 1$ (and all other parameters are as above). The fibre viscosity now decreases monotonically as the fibre passes through the furnace, for all draw ratios.

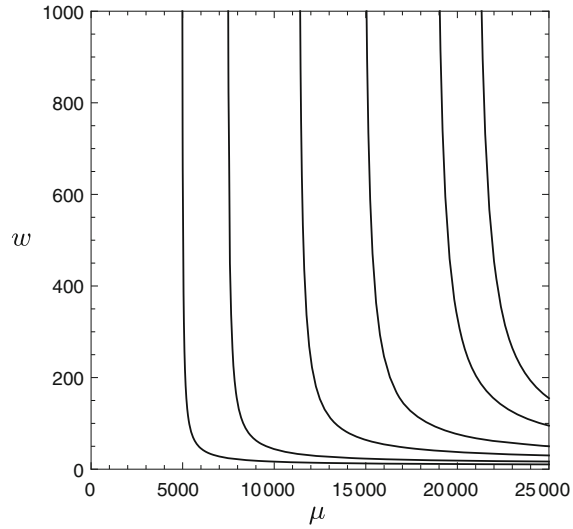

Fig. 13 Phase plane for ambient temperature above glass softening temperature, and parameter β taken to be constant. The fibre viscosity decreases monotonically as the fibre passes through the furnace for all draw ratios

References

1. Carslaw HS, Jaeger JC (1959) Conduction of heat in solids, 2nd edn. Clarendon Press, Oxford
2. Cheng C, Jaluria Y (2007) Modeling of radiation heat transfer in the drawing of an optical fiber with multilayer structure. ASME J Heat Transf 129:342–352
3. Cummings LJ, Howell PD (1999) On the evolution of non-axisymmetric viscous fibres with surface tension, inertia and gravity. J Fluid Mech 389:361–389
4. Filippov A (2011) 27th mathematical problems in industry workshop. Private communication
5. Fitt AD, Furusawa K, Monro TM, Please CP, Richardson DJ (2002) The mathematical modelling of capillary drawing for holey fibre manufacture. J Eng Math 43:201–227
6. Forest GM, Zhou H (2001) Unsteady analyses of thermal glass fibre drawing processes. Eur J Appl Math 12:479–496
7. Frank M, Klar A (2011) Radiative heat transfer and applications for glass production processes. In: Mathematical models in the manufacturing of glass, Lecture Notes in Mathematics. Springer, pp 57–134
8. Geyling FT, Homsy GM (1980) Extensional instabilities of the glass fibre drawing process. Glass Technol 21:95–102
9. Huang H, Miura RM, Wylie JJ (2008) Optical fiber drawing and dopant transport. SIAM J Appl Math 69:330–347
10. Hyun JC (1978) Theory of draw resonance: part I. Newtonian fluids. AIChE J 24:418–422
11. Lee SHK, Jaluria Y (1997) Simulation of the transport processes in the neck-down region of a furnace drawn optical fiber. Int J Heat Mass Transf 40:843–856
12. Lentes FT, Siedow N (1999) Three-dimensional radiative heat transfer in glass cooling processes. Glastech Ber Glass Sci Technol 72:188–196
13. Myers MR (1989) A model for unsteady analysis of preform drawing. AIChE J 35:592–602
14. Paek UC, Runk RB (1978) Physical behavior of the neck-down region during furnace drawing of silica fibers. J Appl Phys 49:4417–4422
15. Papamichael H, Miaoulis IN (1991) Thermal behavior of optical fibers during the cooling stage of the drawing process. J Mater Res 6:159–167
16. Renardy M (2006) Draw resonance revisited. SIAM J Appl Math 66:1261–1269
17. Roy Choudhury S, Jaluria Y (1998) Thermal transport due to material and gas flow in a furnace for drawing an optical fiber. J Mater Res 13:494–503
18. Roy Choudhury S, Jaluria Y, Lee SH-K (1999) A computational method for generating the free-surface neck-down profile for glass flow in optical fiber drawing. Numer Heat Transf Part A 35:1–24
19. Scheid B, Quiligotti S, Tranh B, Gy R, Stone HA (2010) On the (de)stabilization of draw resonance due to cooling. J Fluid Mech 636:155–176
20. Suman B, Kumar S (2009) Draw ratio enhancement in nonisothermal melt spinning. AIChE J 55:581–593
21. Suman B, Tandon P (2010) Fluid flow stability analysis of multilayer fiber drawing. Chem Eng Sci 65:5537–5549
22. Wylie JJ, Huang H (2007) Extensional flows with viscous heating. J Fluid Mech 571:359–370
23. Wylie JJ, Huang H, Miura RM (2007) Thermal instability in drawing viscous threads. J Fluid Mech 570:1–16
24. Yin Z, Jaluria Y (1997) Zonal method to model radiative transport in an optical fiber drawing furnace. ASME J Heat Transf 119:597–603
25. Yin Z, Jaluria Y (2000) Neck down and thermally induced defects in high-speed optical fiber drawing. ASME J Heat Transf 122:351–362